



Article

# Obtaining Polyvinylpyrrolidone Fibers Using the Electroforming Method with the Inclusion of Microcrystalline High-Temperature Phosphates

Marina Vladimirovna Papezhuk<sup>1</sup>, Sergei Nikolaevich Ivanin<sup>1,2</sup> , Roman Pavlovich Yakupov<sup>1,2</sup>, Vladimir Yurievich Buz'ko<sup>1,2</sup>, Igor Vladimirovich Sukhno<sup>2</sup>, Anna Nikolaevna Gneush<sup>2</sup> and Iliya Sergeevich Petriev<sup>1,3,\*</sup>

<sup>1</sup> Faculty of Chemistry and High Technologies, Kuban State University, 350040 Krasnodar, Russia; marina-marina322@mail.ru (M.V.P.); ivanin18071993@mail.ru (S.N.I.); yakupov@sfedu.ru (R.P.Y.); buzkonmr@mail.ru (V.Y.B.)

<sup>2</sup> Laboratory of Advanced Nanobiotechnologies, Kuban State Agricultural University, 350044 Krasnodar, Russia; sukhno\_igor@mail.ru (I.V.S.); gneush.anna@yandex.ru (A.N.G.)

<sup>3</sup> Laboratory of Problems of Stable Isotope Spreading in Living Systems, Southern Scientific Centre of the Russian Academy of Sciences, 344006 Rostov-on-Don, Russia

\* Correspondence: petriev\_iliya@mail.ru

**Abstract:** The results of the synthesis of microcrystalline calcium phosphates such as hydroxyapatite, pyrophosphate, and tricalcium phosphate are presented herein. The influence of the addition of polyvinylpyrrolidone (PVP) on the phase characteristics of the resulting high-temperature ceramic sample is considered. The X-ray results show that hydroxyapatite (HAp) consists of a  $\text{Ca}_5(\text{PO}_4)_3(\text{OH})$  phase, while the sample with the addition of polyvinylpyrrolidone contains  $\beta\text{-Ca}_3(\text{PO}_4)_2$  (65.5%) and  $\beta\text{-Ca}_2\text{P}_2\text{O}_7$  (34.5%) phases calcium phosphates (CPs). IR spectroscopy was used to characterize the compositions of the samples. An important characteristic of the obtained samples is the elemental Ca/P ratio, which was determined via energy-dispersive analysis. The data obtained are consistent with the composition of dental enamel apatites, namely, in the CPs (1.27) and HAp (1.40). SEM was used to study the morphology of the surfaces of hydroxyapatite particles. Polyvinylpyrrolidone polymer fibers were obtained using the electroforming method with the inclusion of CPs in the composition. The fibers were oriented randomly, and nanoscale hydroxyapatite particles were incorporated into the fiber structure. Solubility data of the HAp, CPs, and Fibers in a physiological solution at room temperature and human body temperature were obtained. The solubility of the resulting HAp turned out to be higher than the solubility of the CPs. In turn, the concentration of  $\text{Ca}^{2+}$  in a physiological solution of PVP composite fibers with the inclusion of CPs was lower than that in powdered CPs.

**Keywords:** phosphates; hydroxyapatite; polyvinylpyrrolidone; electrospinning; fibers; SEM; XRD; IR spectroscopy



**Citation:** Papezhuk, M.V.; Ivanin, S.N.; Yakupov, R.P.; Buz'ko, V.Y.; Sukhno, I.V.; Gneush, A.N.; Petriev, I.S. Obtaining Polyvinylpyrrolidone Fibers Using the Electroforming Method with the Inclusion of Microcrystalline High-Temperature Phosphates. *Int. J. Mol. Sci.* **2024**, *25*, 2298. <https://doi.org/10.3390/ijms25042298>

Academic Editor: Jordi Puiggali

Received: 19 January 2024

Revised: 10 February 2024

Accepted: 13 February 2024

Published: 15 February 2024



**Copyright:** © 2024 by the authors. Licensee MDPI, Basel, Switzerland. This article is an open access article distributed under the terms and conditions of the Creative Commons Attribution (CC BY) license (<https://creativecommons.org/licenses/by/4.0/>).

## 1. Introduction

Many companies use various calcium phosphates as the main components of implants in medicine. Issues related to methods of preparation, modification, changes in the phase composition of such compounds, and the physicochemical characteristics of materials based on calcium phosphates remain relevant. Calcium phosphate cements are typical self-hardening ceramic materials used in implant dentistry. Under the influence of environmental conditions, tricalcium phosphate is hydrolyzed to non-stoichiometric hydroxyapatite [1]. Hydroxyapatite (HAp)  $\text{Ca}_{10}(\text{PO}_4)_6(\text{OH})_2$  is the most commonly employed ceramic material in orthopedic and dental therapies. This is due to its preminent presence within the mineral composition of tooth enamel and human bone tissue (60–70%) [1–7].

Hydroxyapatite exhibits high biocompatibility, a complete lack of immunogenicity, carcinogenicity, and slow degradation [8–11]. Obtained by annealing the bones of large-horned cattle, hydroxyapatite is currently used in various biomedical applications. However, this natural (biological) form of hydroxyapatite has drawbacks, including the risk of infection transmission, material rejection, and the possible accumulation of heavy metals in animal bones during their lifetimes [12]. To address these issues, chemically pure synthesized hydroxyapatite can be used. This form offers several advantages, including the satisfaction of ethical and medical considerations. Much attention is paid to synthesis methods, pH control, the use of various additives, and the temperature–time characteristics of annealing during the synthesis of HAp, as these factors impact the end product’s phase composition, structural characteristics, Ca/P ratio, and specific surface area.

Alongside hydroxyapatite, various calcium orthophosphates are used in regenerative medicine. High-temperature calcium orthophosphates and composites, such as  $\alpha$ -,  $\beta$ - $\text{Ca}_3(\text{PO}_4)_2$ ,  $\text{Ca}(\text{H}_2\text{PO}_4)_2$ ,  $\text{Ca}_5(\text{PO}_4)_3(\text{OH})$ ,  $\text{Ca}_4\text{P}_2\text{O}_9$ ,  $\text{Ca}_{10}(\text{PO}_4)_6\text{O}$ ,  $\text{Ca}_{10}(\text{PO}_4)_6\text{F}_2$ , and  $\beta$ - $\text{Ca}_3(\text{PO}_4)_2$ -hydroxyapatite, are traditionally used. The most important property of such compounds is their better solubility in water compared to hydroxyapatite; therefore, pure hydroxyapatite has limited use in the field of hard-tissue regeneration and drug delivery [13]. The solubility of a material allows one to predict its behavior in the environment of the body [14]. If the solubility of a material is less than the solubility of the mineral portion of the bone tissue, then it degrades slowly. If the solubility of a material is higher than the solubility of the corresponding type of bone, then complete resorption occurs. The solubility of calcium phosphate materials increases in the following order: fluorapatite  $\rightarrow$  fluorohydroxyapatite  $\rightarrow$  hydroxyapatite  $\rightarrow$  carbonate hydroxyapatite  $\rightarrow$  tricalcium phosphate  $\rightarrow$  pyrophosphate [15]. Increasing solubility will positively affect the resorbability of calcium phosphate materials [16–18]. But in turn, excessively high solubility can lead to voids in the implanted material, which cannot be filled quickly enough with the body’s natural HAp. Therefore, hydroxyapatite is typically incorporated into composites with calcium orthophosphates or polymers [19–22]. In addition, such a material will be most similar to natural bone tissue [23], which is a hydroxyapatite–collagen composite.

A wide range of polymers can be utilized for the production of such fibers. In particular, biocompatible polymers are of great interest as they meet several criteria, including a lack of a propensity to induce local inflammatory reactions, allergies, or toxic effects. Additionally, these polymer materials can biodegrade in the presence of living tissues and biological fluids. In tissue regeneration, these polymers are especially useful, as they reduce the risk of implant rejection by the body’s immune system. Examples of such polymers include polycaprolactone (PCL), polyvinyl alcohol (PVA), polyvinylpyrrolidone (PVP), and chitosan (CHS) [23–28]. These polymers can be used as implantable scaffolds for ceramic. The removal of the scaffold from the body does not require surgery, as the polymer is absorbed and degraded by the body [29]. The inclusion of ceramic materials in the polymer matrix makes it possible to control the rates of degradation and resorption [30].

Recently, composite materials in the form of non-woven fibers with ceramic additives included in them have been of particular interest. The electrospinning method makes it possible to obtain non-woven materials with fibers ranging in size from micrometers to nanometers [31,32]. This range of fiber sizes allows for greater specific surface area and flexibility in performing surface functions than any other known form of material [33]. Due to these outstanding properties, polymer nanofibers are optimal candidates for many important applications in biomedical fields: polymer nonwoven fibers are used in drug delivery systems [16], and nonwoven fibers have a large surface area suitable for cell attachment [33]. Polyvinylpyrrolidone-based fibers are of particular interest. The main advantage of PVP is its biodegradability in physiological environments. Non-toxic and biocompatible PVP does not have a negative effect on animal organisms and has an optimal absorption rate and non-toxic decomposition products [34].

The aim of this work was to study the bioresorbability of synthesized HAp and CPs as well as the composite fibers for their further use in regenerative medicine.

## 2. Results

Figure 1 shows the results of X-ray phase analysis for samples calcined at 900 °C for 2 h.

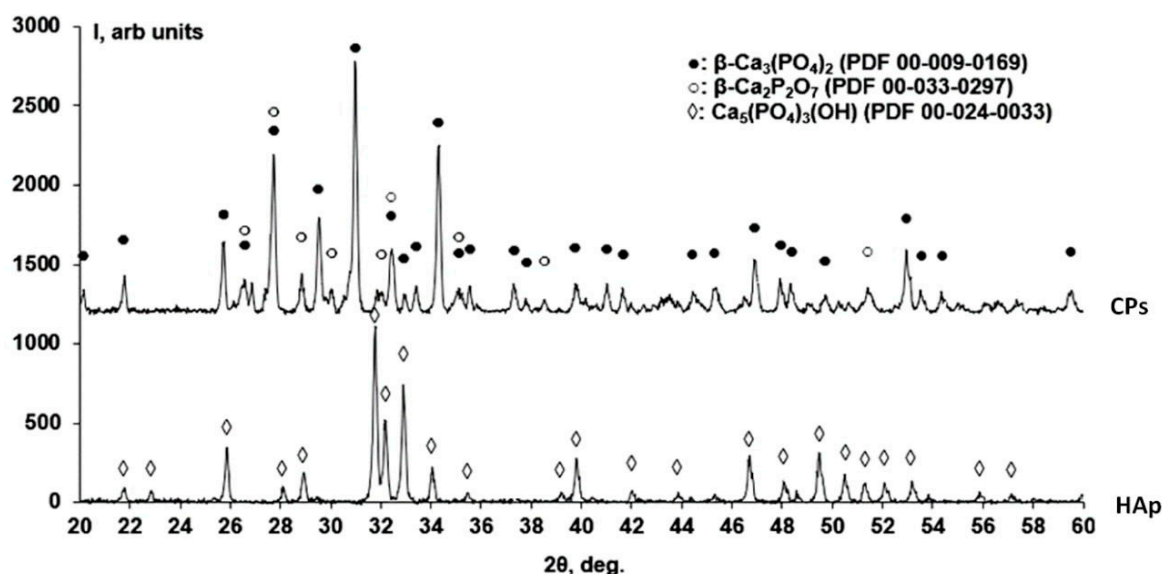


Figure 1. X-ray phase analysis of HAp and CPs.

The X-ray results show that the sample of hydroxyapatite consists of a  $\text{Ca}_5(\text{PO}_4)_3(\text{OH})$  phase (PDF 00-024-0033), while the CPs sample with the addition of polyvinylpyrrolidone contains  $\beta\text{-Ca}_3(\text{PO}_4)_2$  (PDF 00-009-0169) and  $\beta\text{-Ca}_2\text{P}_2\text{O}_7$  (PDF 00-033-0297) phases.

The crystal lattice parameters for  $\text{Ca}_5(\text{PO}_4)_3(\text{OH})$ ,  $\beta\text{-Ca}_3(\text{PO}_4)_2$  and  $\beta\text{-Ca}_2\text{P}_2\text{O}_7$  are given in Table 1.

Table 1. Lattice parameters of  $\text{Ca}_5(\text{PO}_4)_3(\text{OH})$ ,  $\beta\text{-Ca}_3(\text{PO}_4)_2$ , and  $\beta\text{-Ca}_2\text{P}_2\text{O}_7$ .

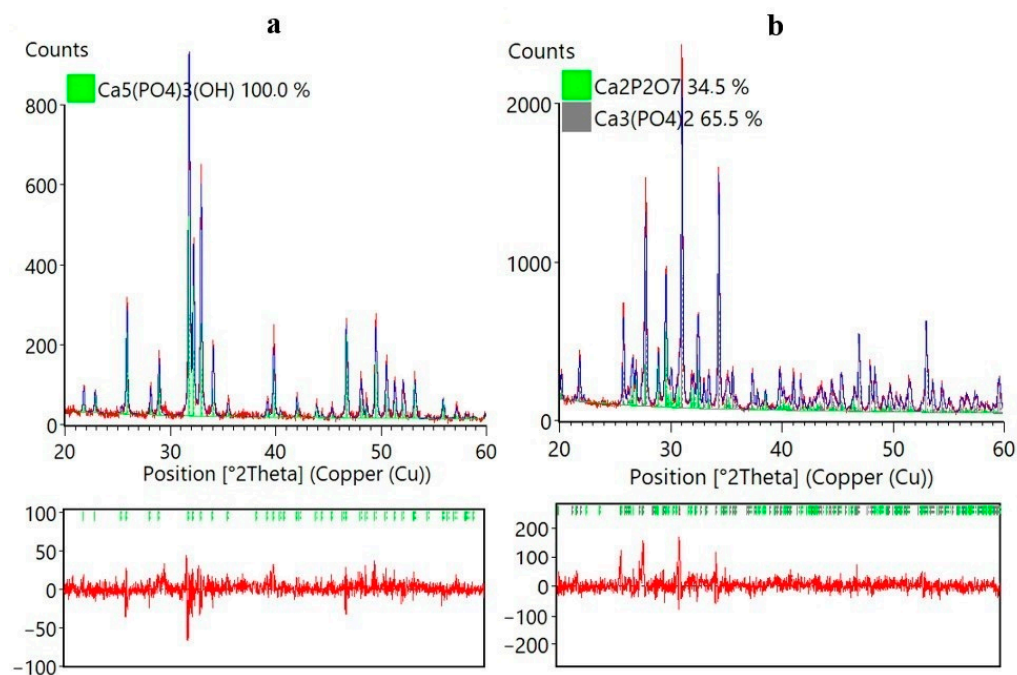
Chemical Formula	Crystal System	Space Group	a, Å	b, Å	c, Å	Alpha, °	Beta, °	Gamma, °
$\text{Ca}_3(\text{PO}_4)_2$	Rhombohedral	R-3c	10.4290	10.4290	37.3800	90	90	120
$\text{Ca}_2\text{P}_2\text{O}_7$	Tetragonal	P41	6.6840	6.6840	24.1450	90	90	90
$\text{Ca}_5(\text{PO}_4)_3(\text{OH})$	Hexagonal	$\text{P6}_3/\text{m}$	9.4320	9.4320	6.8810	90	90	120

Figure 2 shows the Rietveld refinement data for the X-ray diffraction data obtained for HAp (Figure 2a) in the space group  $\text{P6}_3/\text{m}$  (a) for CPs refined in space groups R-3c and P41, respectively (Figure 2b).

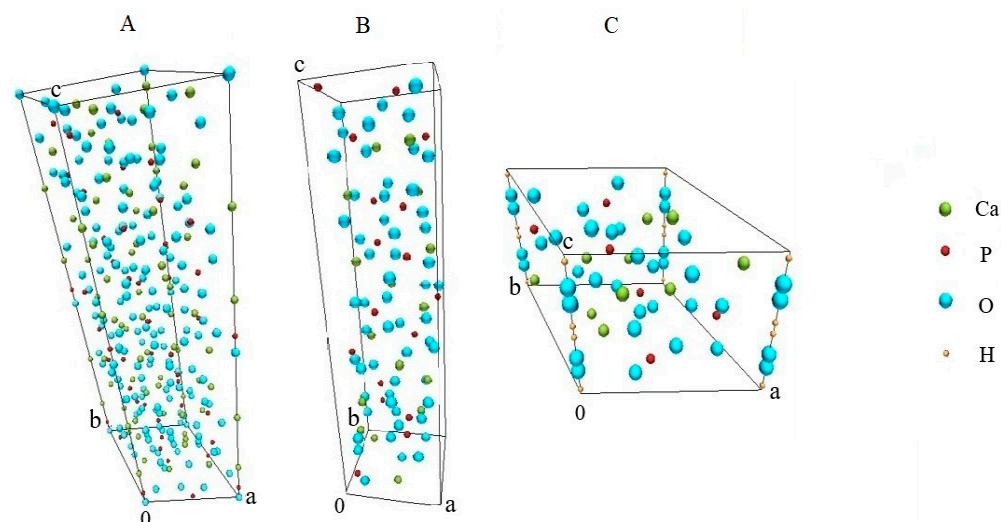
From Figure 2b, it can be gleaned that the CPs consist of 34.5%  $\beta\text{-Ca}_2\text{P}_2\text{O}_7$  phase and 65.5%  $\beta\text{-Ca}_3(\text{PO}_4)_2$  phase. The Goodness-of-Fit (GOF) parameter for the HAp sample has a value of 1.67, while that for the CP sample it is 1.79.

Figure 3 shows images of the structures of the researched compounds, i.e.,  $\text{Ca}_5(\text{PO}_4)_3(\text{OH})$  (a),  $\beta\text{-Ca}_3(\text{PO}_4)_2$  (b), and  $\beta\text{-Ca}_2\text{P}_2\text{O}_7$  (c).

Hydroxyapatite (Figure 3A) crystallizes with hexagonal symmetry, corresponding to space group  $\text{P6}_3/\text{m}$ . In the HAp crystal lattice,  $\text{PO}_4^{3-}$  tetrahedra are connected by  $\text{Ca}^{2+}$  bridges. The  $\text{OH}^-$  ions are aligned along the sixfold lattice axis bounded by the  $\text{Ca}^{2+}$  and  $\text{PO}_4^{3-}$  columns, forming the so-called “apathetic channel”. Phosphate  $\beta\text{-Ca}_3(\text{PO}_4)_2$  (Figure 3B) crystallizes in the polar trigonal space group R-3c. Dicalcium diphosphate (Figure 3C) consists of  $\text{P}_2\text{O}_7^{2-}$  groups connected by  $\text{Ca}^{2+}$  cations. It crystallizes in the tetragonal symmetry group P41.

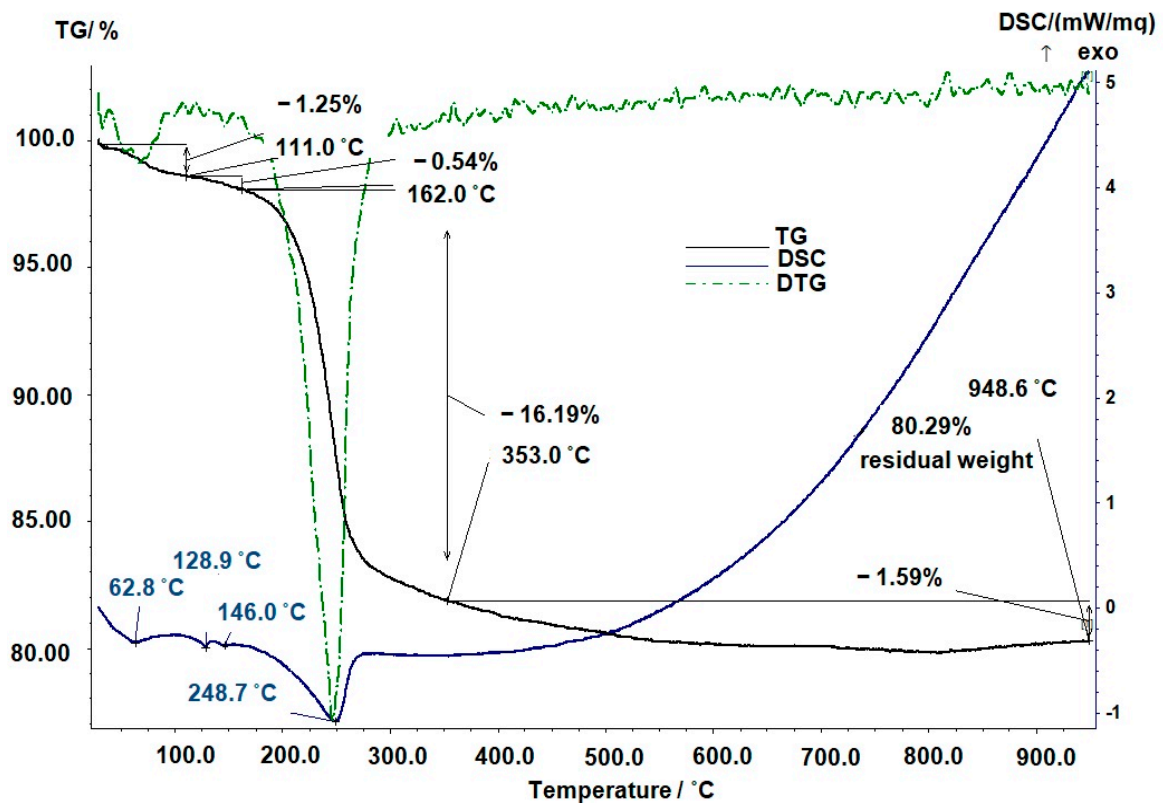


**Figure 2.** Refinement via the Rietveld method of X-ray diffraction data obtained for  $\text{Ca}_5(\text{PO}_4)_3(\text{OH})$  in the space group  $P6_3/m$  (a) and for  $\beta\text{-Ca}_3(\text{PO}_4)_2$  and  $\beta\text{-Ca}_2\text{P}_2\text{O}_7$  refined in space groups  $R\text{-}3c$  and  $P41$ , respectively (b). The red solid line and blue solid line represent the experimental and calculated intensities, respectively, and the red line below represents the difference between them. Green marks indicate the positions of the Bragg peaks.



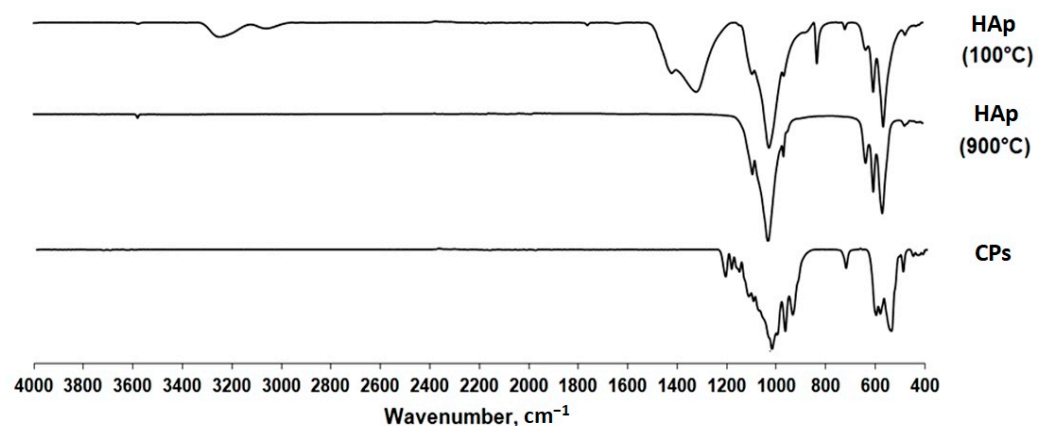
**Figure 3.** Structures of the researched compounds, according to CIF files:  $\text{Ca}_5(\text{PO}_4)_3(\text{OH})$  (A),  $\beta\text{-Ca}_3(\text{PO}_4)_2$  (B), and  $\beta\text{-Ca}_2\text{P}_2\text{O}_7$  (C).

Figure 4 shows the TG, DTG, and DSC curves of hydroxyapatite dried at  $100\text{ }^{\circ}\text{C}$ . The HA powder was heated from room temperature to  $1000\text{ }^{\circ}\text{C}$ . In the figure, when the temperature reaches  $111\text{ }^{\circ}\text{C}$ , weight loss is visible on the TG curve. In the range of  $200\text{--}350\text{ }^{\circ}\text{C}$ , HAp powder quickly loses weight. Further heating did not lead to changes in weight. The total mass loss was 19.71%.



**Figure 4.** Thermogram of a hydroxyapatite sample dried at 100 °C indicating the curves: the black solid line is mass loss versus temperature (TG); the green dashed line is differential curve corresponding to the maximum rate of change in sample mass (DTG); the blue solid line is first derivative of temperature for phase transitions (DSC).

The analysis of the functional groups in the samples was conducted using infrared spectroscopy (Figure 5). Based on literature data [2,35,36], the main characteristic vibration frequencies of  $\text{PO}_4^{3-}$  and  $\text{OH}^-$  groups were determined for the synthesized samples.



**Figure 5.** IR spectra of HAp (100 °C), HAp (900 °C), and CPs.

In the IR spectrum of HAp (100 °C) (Figure 5) dried at 100 °C, nitrate group ( $\text{NO}_3^-$ ;  $1315\text{ cm}^{-1}$ ) and carbonate group ( $\text{CO}_3^{2-}$ ;  $1416\text{ cm}^{-1}$  and  $827\text{ cm}^{-1}$ ) bands are present.

The vibrations of the  $\text{OH}^-$  group in HAp (900 °C) (Figure 5) are located at  $3570\text{ cm}^{-1}$  and  $631\text{ cm}^{-1}$  [37,38]. The band around  $962\text{ cm}^{-1}$  is explained by the non-degenerate symmetric vibration of the P-O bond in the phosphate group [39]. The weak peak at approximately  $474\text{ cm}^{-1}$  indicates the doubly degenerate bending vibration of the P-O

bond in the phosphate group,  $\nu^2$ . The most intense peak of phosphate vibrations at  $1094\text{ cm}^{-1}$  can be explained by the triply degenerate asymmetric stretching vibrations of the P-O bond,  $\nu^3$ . The band at  $1020\text{ cm}^{-1}$  is also explained by stretching vibrations of the phosphate ion. The sharp peaks at  $559\text{ cm}^{-1}$  and  $600\text{ cm}^{-1}$  are associated with the  $\nu^4$  mode of the O-P-O bond. The band at  $962\text{ cm}^{-1}$  is associated with the symmetric stretching  $\nu^1$  mode of the P-O bond, while the two strong bands at  $1033\text{ cm}^{-1}$  and  $1094\text{ cm}^{-1}$  are associated with the  $\nu^3$  mode.

The IR spectrum of the CPs (Figure 5) corresponds to the spectrum of the HAp sample without additives, calcined at  $900\text{ }^\circ\text{C}$ , except for additional signals at  $943\text{ cm}^{-1}$  and  $727\text{ cm}^{-1}$ . These vibrations represent *vas* and *vs* modes of P-O-P in the  $\text{P}_2\text{O}_7^{2-}$  ion, respectively [40]. Functional groups are present in the pyrophosphate phase [33]. The bands at  $1213\text{ cm}^{-1}$  and  $1157\text{ cm}^{-1}$  can be attributed to the stretching vibrations of the P=O ion in  $\text{PO}_4^{3-}$  [41]. Signals from the OH group are absent in the spectrum.

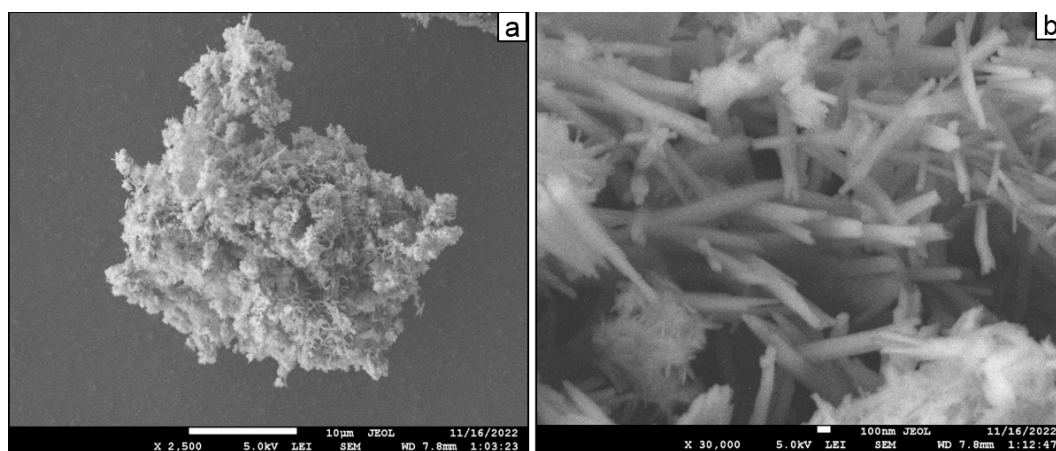
The results of IR spectroscopy are consistent with the data from thermal and X-ray phase analysis.

Scanning electron microscopy (SEM) was used to study the microstructures, particle sizes, and surface morphology of samples annealed at different temperatures. Microstructure was studied in the detection-of-secondary-electrons mode. The advantage of using the secondary electron detection mode is that it grants one the ability to study surface morphology with the dependence of contrast on relief [42,43].

Figure 6 shows SEM photographs of the synthesized samples.

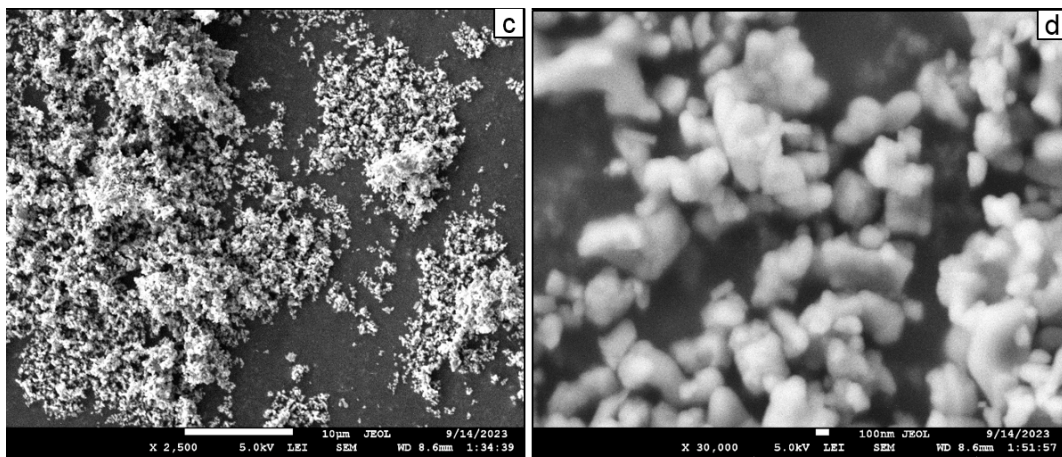
Based on the obtained photographs of the microstructure of the studied HAp and CPs, histograms of particle size distribution were constructed (Figure 7).

To determine the qualitative composition of the synthesized samples and confirm the absence of impurities, energy-dispersive X-ray microanalysis (EDX) was carried out using an IncaX-sight energy-dispersive detector (Oxford Instruments, Abingdon, England) installed on a JEOL JSM-7500F scanning electron microscope (JEOL, Tokyo, Japan). The X-ray spectral analysis method allows for both the qualitative and quantitative analysis of samples without destroying their integrity [44,45]. To carry out energy-dispersive analysis, the synthesized samples were pressed into tablets (Figure 8f) using a pressure of  $5\text{ tons/cm}^2$ . Figure 8 shows the scanning area of the sample,  $30 \times 30\text{ }\mu\text{m}$  (a); a map of the distribution of elements in the tablet of the HAp sample, namely, O (b), P (c), and Ca (d); and the EDA spectrum of the HAp sample (e). It is shown that the distribution of elements was uniform over the entire area of the tablet. The study of the samples' CPs was carried out similarly. The results of elemental analysis are summarized in Table 2.

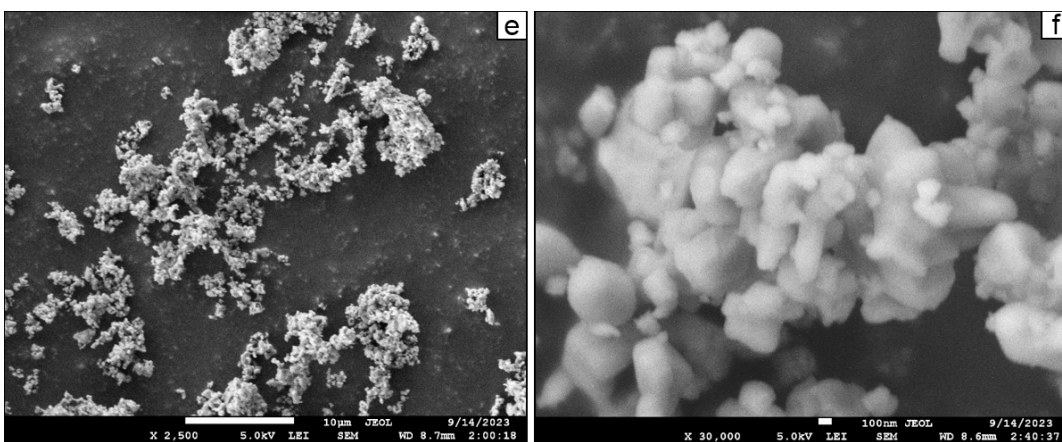


HAp (100 °C)

Figure 6. Cont.



HAp (900 °C).



CPs.

Figure 6. SEM photographs (2500 $\times$ , 30,000 $\times$ ) of the microstructures of the synthesized HAp (100 °C)—(a,b); HAp (900 °C)—(c,d); CPs—(e,f).

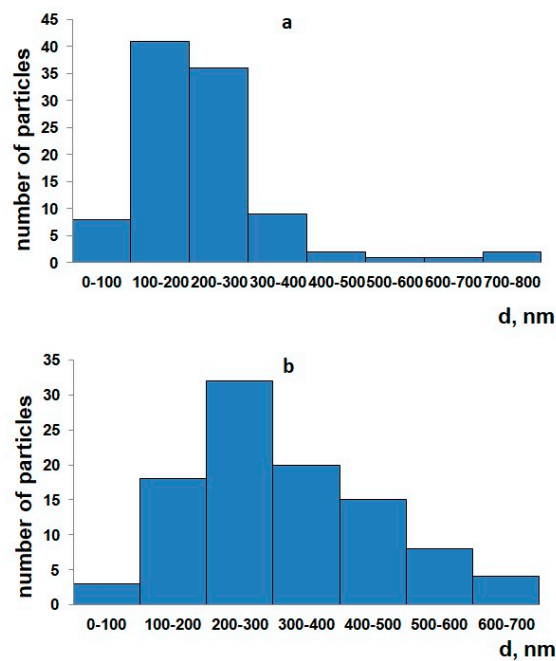
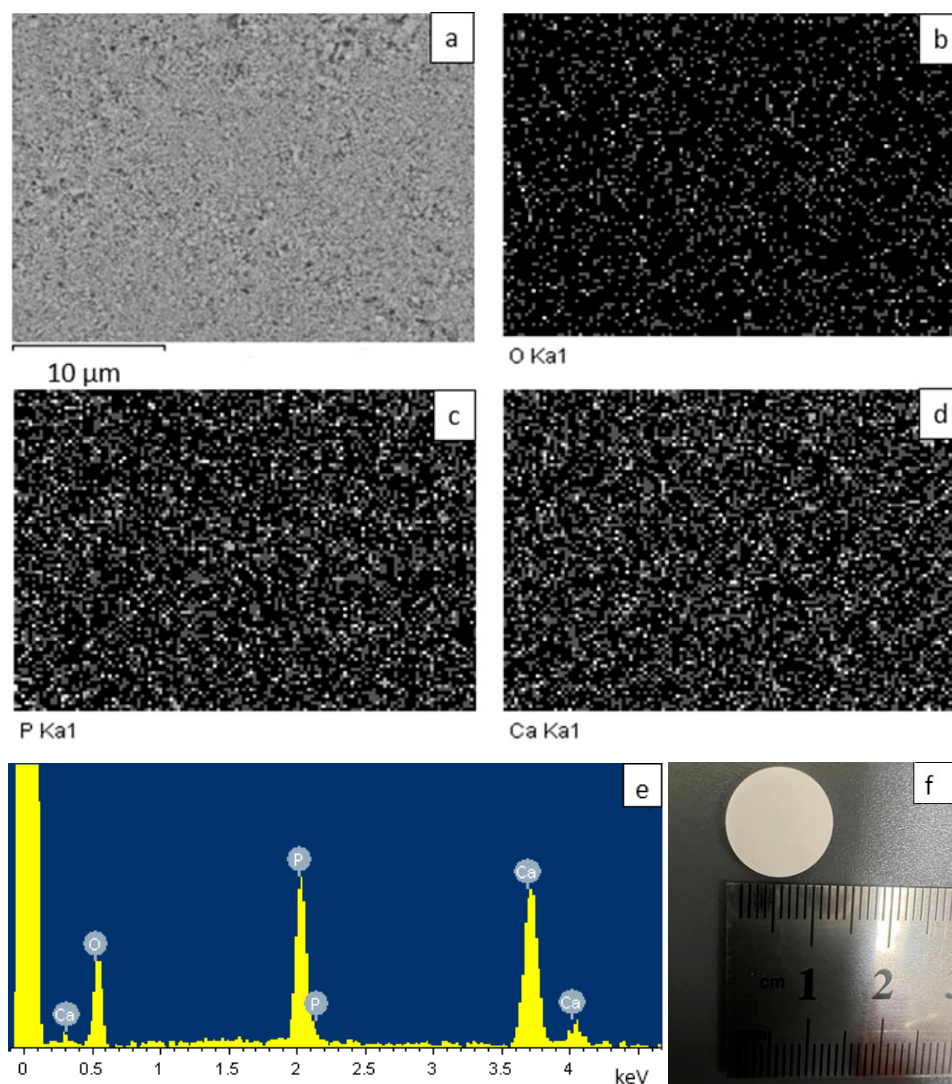


Figure 7. Histogram of particle size distribution for HAp (a) and CPs (b).



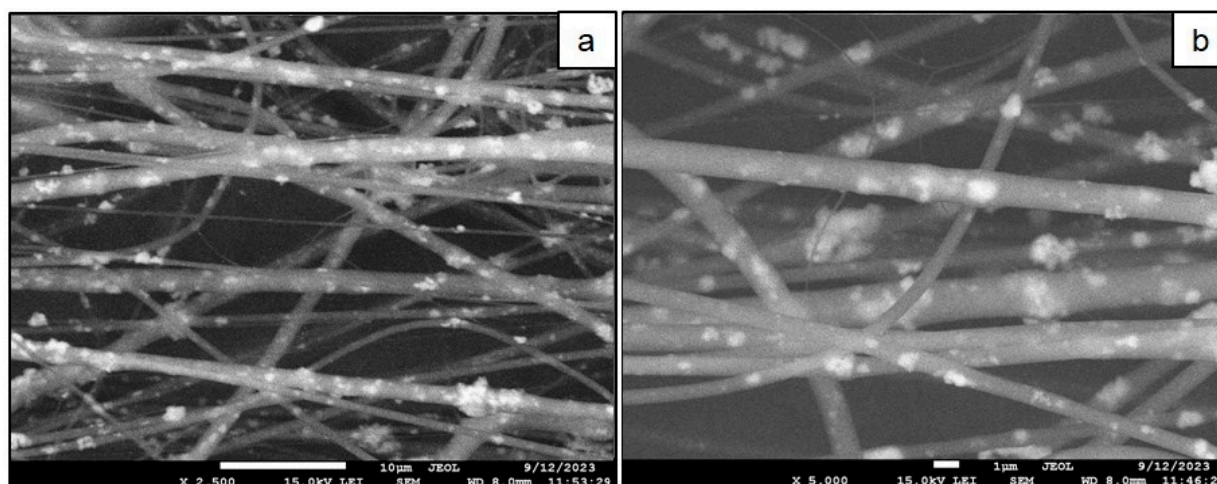
**Figure 8.** EDA analysis results: sample-scanning area (a); distribution of elements in the sample—O (b), P (c), and Ca (d); EDA spectrum (e); appearance of a compressed tablet (f).

**Table 2.** Elemental composition (at%) of the synthesized samples.

	Samples	
	CPs	HAp
Ca	19.22	23.04
P	15.17	16.45
O	65.62	60.51
Ca/P	1.27	1.4

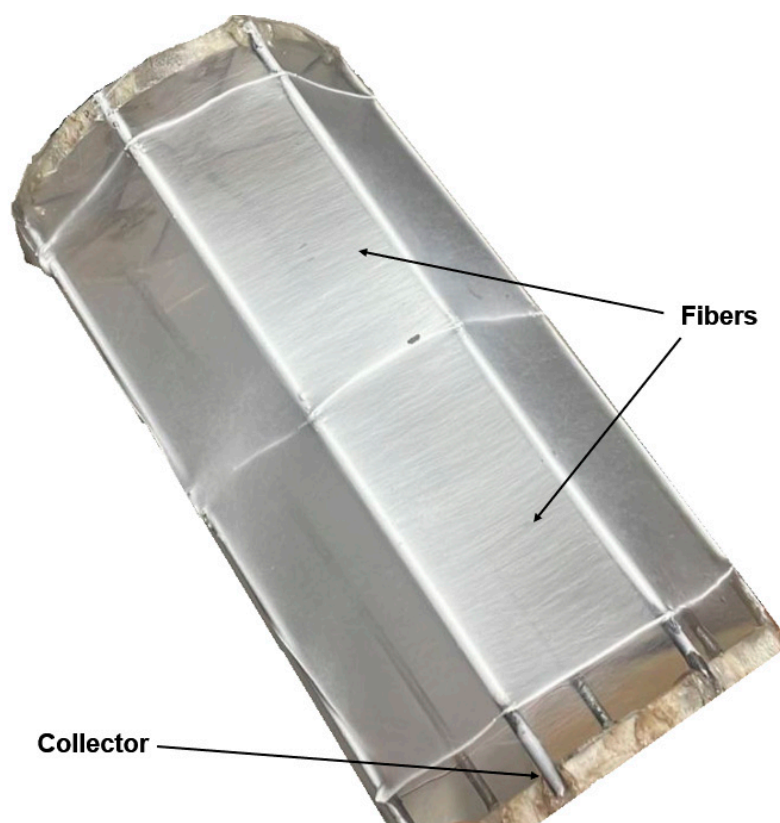
It is worth noting that the CP sample does not contain carbon atoms, which indicates that the entire polymer additive burned out during the annealing of the sample.

Figure 9 shows photographs of the CPs included in the PVP fibers. At magnifications of 2500 $\times$  and 5000 $\times$ , it can be seen that the fibers have a diameter of up to 2  $\mu\text{m}$ . The powder of the CPs is evenly distributed throughout the volume of the fibers.



**Figure 9.** Photographs magnified 2500× (a) and 5000× (b) of the microstructures of the CPs fibers.

Figure 10 shows an image of a collector with composite fibers sprayed onto it.



**Figure 10.** Photo of fibers transferred onto a collector.

The fibers formed a homogeneous mat (Figure 10). The absence of defects on the surfaces of the resulting polymer fibers indicates the optimal selection of parameters for producing micron fibers via electrospinning. As can be seen in Figure 9, the fibers are randomly oriented and have a smooth surface.

The resorption capacity of a material is determined using solubility values. Table 3 shows the solubility values of the samples, namely, HAp, CPs, and Fibers (CPs), in a physiological solution at room temperature ( $20 \pm 1$  °C) and human body temperature ( $37 \pm 1$  °C). The content of  $\text{Ca}^{2+}$  ions in the solution was determined using trilonometric titration in the presence of eriochrome black T with an ammonia buffer (pH 9–10) [46].

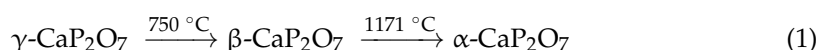
**Table 3.** The solubility of sample powders in physiological solution at pH 7,  $\omega$  (NaCl) = 0.9%.

Samples	Concentration of Ca <sup>2+</sup> , mol/L	
	20 °C	37 °C
HAp	1·10 <sup>-3</sup>	1.5·10 <sup>-3</sup>
CPs	2.5·10 <sup>-4</sup>	3.1·10 <sup>-4</sup>
Fibers (CPs)	1·10 <sup>-4</sup>	1.2·10 <sup>-4</sup>

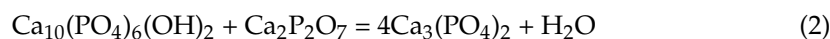
### 3. Discussion

The powders of the studied samples were synthesized in the laboratory via chemical deposition from a solution. When performing this synthesis method in an alkaline environment, it is critical to understand that, depending on the synthesis conditions, carbonate-containing hydroxyapatite is often obtained. Substitution groups can cause characteristic changes in lattice parameters, crystallinity, crystal symmetry, thermal stability, morphology and solubility, and physical, chemical, and biological characteristics. Accordingly, it should be taken into account that CO<sub>2</sub> is released from the sample at a temperature of 450–950 °C, and to obtain Ca<sub>10</sub>(PO<sub>4</sub>)<sub>6</sub>(OH)<sub>2</sub>, it is necessary to carry out subsequent high-temperature annealing of the sample. We studied samples of HAp dried at 100 °C, HAp annealed at 900 °C, and CPs obtained using a similar synthesis method. The difference was the use of a polymer additive (PVP) during the synthesis.

In the X-ray diffraction pattern (Figure 1) of HAp, reflections belonging to the Ca<sub>5</sub>(PO<sub>4</sub>)<sub>3</sub>(OH) phase (PDF 00-024-0033) can be observed. In the X-ray diffraction pattern of the CPs, two phases can be identified, namely, calcium phosphate Ca<sub>3</sub>(PO<sub>4</sub>)<sub>2</sub> (PDF 00-009-0169) and calcium pyrophosphate β-Ca<sub>2</sub>P<sub>2</sub>O<sub>7</sub> (PDF 00-033-0297), which is consistent with the data [47]. To quantify the phases in the CPs, the Rietveld method [48] was used (Figure 2). We used HighScore Plus version 3.0e (3.0.5) and CIF files (Figure 3) from the following works: for Ca<sub>5</sub>(PO<sub>4</sub>)<sub>3</sub>(OH), [49]; for β-Ca<sub>3</sub>(PO<sub>4</sub>)<sub>2</sub>, [50]; and for the β-Ca<sub>2</sub>P<sub>2</sub>O<sub>7</sub> phase, [51]. CPs is a two-phase powder with a phase ratio of 34.5%:65.5% for β-Ca<sub>2</sub>P<sub>2</sub>O<sub>7</sub> and β-Ca<sub>3</sub>(PO<sub>4</sub>)<sub>2</sub>, respectively (Figure 2). Apparently, the polymer additive of PVP affects the thermal stability of hydroxyapatite. As a result of thermal treatment, calcium hydrogen phosphate (CaHPO<sub>4</sub>) is formed from brushite (CaHPO<sub>4</sub>·2H<sub>2</sub>O). In turn, at about 700 °C, calcium hydrogen phosphate (CaHPO<sub>4</sub>) converts to calcium pyrophosphate (Ca<sub>2</sub>P<sub>2</sub>O<sub>7</sub>). According to X-ray diffraction studies of Ca<sub>2</sub>P<sub>2</sub>O<sub>7</sub>, it exists in three different forms depending on the temperature, according to Equation (1) [52–54].



During high-temperature sintering at around 900 °C, the formation of whitlockite occurs, according to Equation (2) [55].



Thus, under these synthesis conditions, high-temperature calcium orthophosphates are formed. It should be noted that for the method of synthesis used and the corresponding calcination temperature, the Ca<sub>3</sub>(PO<sub>4</sub>)<sub>2</sub> phase may form as an impurity phase in both samples, which was also confirmed in [2,35].

According to the results of thermogravimetric (TG) analysis (Figure 4), the mass of hydroxyapatite (HAp (100 °C)) powder without additives decreased by 19.71% when HAp (100 °C) was heated to 948.6 °C. With further heating, the substance remained thermally stable [47,56]. The process of the thermal decomposition of hydroxyapatite samples obtained without additives and preliminarily dried at 100 °C can be divided into stages. The first is the removal of sorbed water [57,58] and carbon dioxide (1.25% 111 °C; 0.54% 162 °C), and the second is the decomposition of ammonium nitrate and

hydroxyapatite carbonate with the elimination of  $\text{CO}_2$  (16.19% at 353 °C). The peak on the DTG (Figure 4) curve at 248 °C is associated with the decomposition of ammonium nitrate.

As expected, when considering the IR spectrum (Figure 5) of HAp dried at 100 °C, this spectrum contained peaks at  $1416\text{ cm}^{-1}$  and  $827\text{ cm}^{-1}$ , correlated with the  $\text{CO}_3^{2-}$  group [39]. Their presence is due to the high activity of  $\text{Ca}(\text{OH})_2$  and the presence of carbon dioxide in the air. In addition, the  $\text{NO}_3^-$  group is also present in the IR spectrum of HAp (100 °C). Absorption bands of the  $\text{NO}_3^-$  group are also present in the IR spectrum in the regions of  $1315\text{ cm}^{-1}$  and  $827\text{ cm}^{-1}$ . When the samples were calcined at a temperature of 250–300 °C, ammonium nitrate, which was sorbed on the surface of the sample, decomposed; accordingly, the  $\text{NO}_3^-$  signal disappeared in the IR spectrum of HA annealed at 900 °C. The appearance of additional signals in the IR spectrum of an HA sample obtained with the addition of PVP may indicate the appearance of another phase. The signals at  $943$  and  $727\text{ cm}^{-1}$  belong to *vas* P-O-P and *va* P-O-P in the  $\text{P}_2\text{O}_7^{2-}$  ion, respectively [33,40].

Analysis of the obtained microstructure photographs (Figure 6) led us to the conclusion that the synthesized sample HAp (100 °C) consisted of agglomerates with a size of 20–30  $\mu\text{m}$  (Figure 6a), consisting of smaller particles. At a magnification of 30,000 $\times$ , it can be seen that the agglomerates of the hydroxyapatite sample consist of two fractions of thread-like particles: one with a diameter of about 100 nm and a length of several microns and one with a diameter of more than 10–20 nm (Figure 6b). Figure 6c,d show microstructure photographs of HAp (900 °C) obtained at magnifications of 2500 $\times$  and 30,000 $\times$ , respectively. It should be noted that upon calcination of the hydroxyapatite sample at 900 °C, the sintering of thread-like particles occurs, followed by the formation of a microcrystalline homogeneous powder. Figure 6e,f show photographs of the CPs. At a magnification of 30,000 $\times$ , the CPs consists of agglomerates of sintered submicron-sized particles with a non-uniform shape.

The molar ratio of Ca/P in the mineral phase of bone tissue ranges from 1.37 to 1.67. [18,59,60]. In our case, the molar ratio of CPs is 1.27, and that for HAp is 1.4 (Figure 8e, Table 2). Such a ratio corresponds to the bone composition of tooth enamel (1.33–2.00) [61].

Synthetic hydroxyapatite has low solubility, and it is limitedly used as an implant material in its pure form [13,62]. Therefore, additional manipulations are required to increase the overall solubility (bioresorbability) of hydroxyapatite-based materials. The rate of dissolution of a material depends on the magnitude of its physical and chemical characteristics, such as its composition, specific surface area, and the presence of defects in the crystal lattice [63]. In practice, the bioactivity of a material is characterized by the rapidity of fusion with the bone tissue of the body through the formation of HAp on the surface of the material as a result of the hydrolysis of calcium phosphates or due to the deposition of HAp onto the surface of the material from a supersaturated intercellular fluid [64–66]. Data on the solubility of the samples are given in Table 3. The solubility of CPs turned out to be lower than the solubility of HAp by an order of magnitude. Coarse-crystalline ceramics based on  $\beta\text{-Ca}_3(\text{PO}_4)_2$  and  $\beta\text{-Ca}_2\text{P}_2\text{O}_7$  are resorbed more slowly, which can be attributed to the difference in the particle size of HAp and CPs. A histogram of the particle size distribution is shown in Figure 7. From the data, it can be gleaned that HAp consists mainly of particles with a size of 100–300 nm, and CPs consists of particles with a size of 200–400 nm. The  $\text{Ca}^{2+}$  concentration value (mol/L) in the physiological solution of PVP composite fibers with the inclusion of CPs was lower than that of powder CPs, which is associated with the formation of hydrogel when PVP fibers swell in a physiological solution. Thus, PVP makes it difficult for free calcium ions to escape from the surfaces of the fibers into the solution.

## 4. Materials and Methods

### 4.1. Materials

$\text{Ca}(\text{NO}_3)_2 \cdot 4\text{H}_2\text{O}$  (purum),  $(\text{NH}_4)_2\text{HPO}_4$  (pro analysi), 25% aqueous ammonia solution  $\text{NH}_4\text{OH}$  (purissimum speciale), and polyvinylpyrrolidone (PVP, Mw 40,000) were pur-

chased from Vecton Company (Krasnodar, Russia). Standard titer EDTA- $\text{Na}_2$  (0.1 N) and Eriochrome black T (pro analysi) were purchased from LenReaktiv (St. Petersburg, Russia).

#### 4.2. Calcium Phosphate Synthesis

Synthesis of hydroxyapatite without additives was carried out via precipitation from solution according to the procedure described in [67,68]. The scheme of the synthesis of hydroxyapatite and hydroxyapatite with additives is shown in Figure 11.

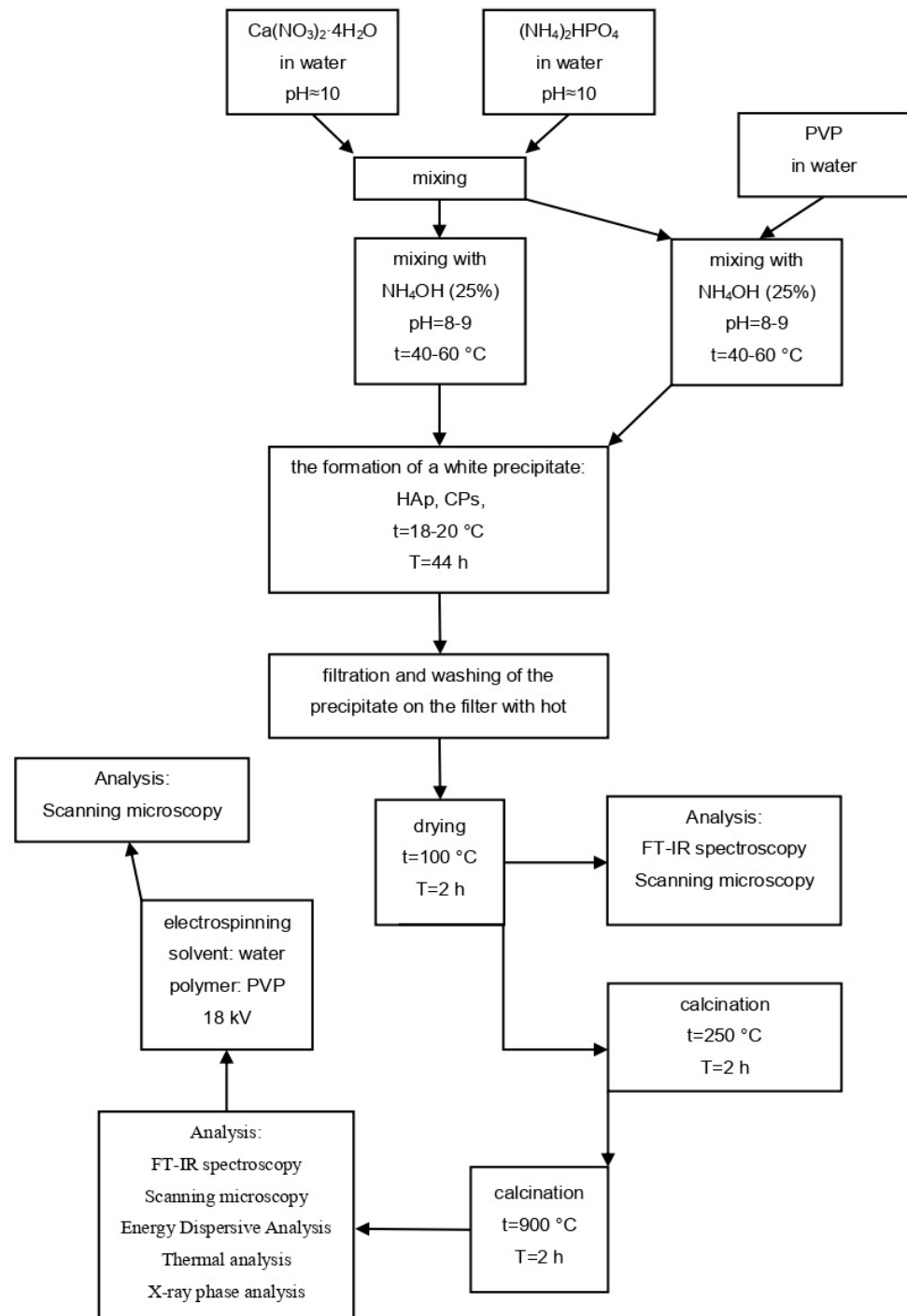


**Figure 11.** Flow chart depicting the steps of the study.

To obtain the hydroxyapatite (hereafter referred to as HAp), a stoichiometrically required amount of calcium (II) nitrate was dissolved in a specific volume of calcium nitrate

solution according to our calculations. The stoichiometric Ca/P elemental ratio should be 1.67, which corresponds to the element ratio in biogenic hydroxyapatite [69]. Next, under intensive stirring, an ammonium hydrogen phosphate solution was added, and the pH of the reagents was then adjusted to 10 using a concentrated ammonia solution ( $\rho = 0.903 \text{ g/mL}$ ). The solution was stirred using a magnetic stirrer for 2 h while monitoring the pH and temperature; then, the solution was left to stand for 44 h. The equation of the reaction is shown in (3):



Then, the precipitate was filtered using a Buchner funnel, washed with hot distilled water on the filter, and dried at  $100^\circ\text{C}$  for 2 h and at  $250^\circ\text{C}$  for 1 h. HAp was selected for analysis during the drying stage at  $100^\circ\text{C}$ . After drying, the obtained sample was annealed in a muffle furnace at  $900^\circ\text{C}$  for 2 h. A modified synthesis method was also used to obtain CPs. PVP polymer was added to vary the phase composition of the material.

#### 4.3. Electrospinning of Fibers

A 10% polymeric viscous solution of polyvinylpyrrolidone in ethanol was prepared. A total of 0.02 g of CPs was dissolved in 0.3 g of the polyvinylpyrrolidone solution. A schematic of the needleless electrospinning installation is shown in Figure 12.

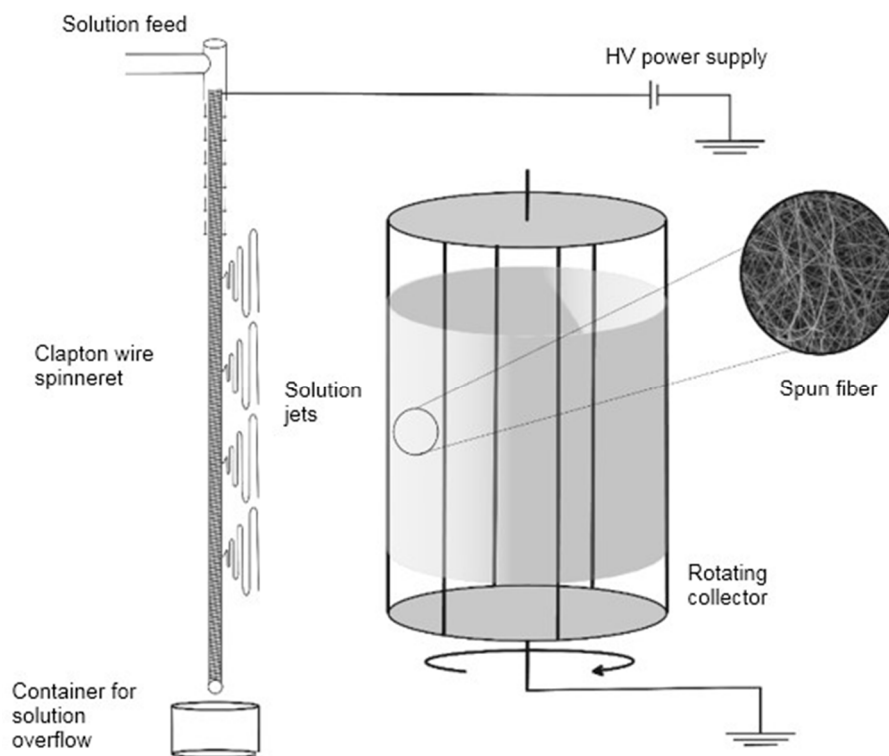


**Figure 12.** Scheme of needleless electrospinning setup.

A sample of hydroxyapatite was ground in an agate mortar. Double-distilled water was used as a solvent. The prepared solutions were used for electrospinning. In this study, we used a needleless electrospinning design that allows the formation of fibers from a solution flowing under the influence of gravity along a vertically oriented spinning electrode—a metal wire in which a 0.2 mm wire is wound on a 1 mm wire. The resulting fibers were collected on a grounded rotating cylindrical collector located 10 cm from the spinning electrode. The applied voltage was 18 kV, and the forming electrode and the collector were created by connecting to a high-voltage source. The fibers produced were collected on a rotating collector electrode consisting of eight metal rods that, when in

motion, acted as a cylindrical surface. After the electrospinning process, the composite fibers were air-dried for 24 h.

#### 4.4. Experimental Method

To determine the phase composition of hydroxyapatite samples, powder X-ray phase analysis was carried out on an X-ray diffractometer XRD-7000 (Shimadzu, Japan). The samples were studied in the range of  $2\theta$  angles from  $20^\circ$  to  $60^\circ$ , using Cu  $K\alpha$  radiation ( $\lambda = 1.5406 \text{ \AA}$ ). XRD measurements were taken at room temperature.

The thermal degradation of the samples was studied using a Netzsch STA 409 PC/PG instrument in the range of  $25\text{--}1000^\circ\text{C}$  in an open platinum–rhodium crucible in air using  $\text{Al}_2\text{O}_3$  as an inert standard. The heating rate was  $10^\circ\text{C}$  per minute.

The functional groups in the synthesized hydroxyapatite samples were determined using Fourier transform infrared spectroscopy (FTIR). FTIR spectra were obtained using a Fourier transform spectrophotometer, VERTEX 70 (BRUKER, Ettlingen, Germany), in the middle-infrared range in the frequency range of  $400\text{--}4000 \text{ cm}^{-1}$ .

Measurement of the fiber size as well as analysis of the surface morphology of hydroxyapatite samples were carried out using a JEOL JSM-7500F ultra-high-resolution scanning electron microscope (JEOL, Tokyo, Japan).

A histogram of particle size distribution was constructed using the ImageJ 1.52u software product.

Elemental analysis of hydroxyapatite samples was carried out using an IncaX-sight energy-dispersive detector installed on an electron microscope.

The solubility of the samples was determined in physiological solution according to the total content of  $\text{Ca}^{2+}$  ions. The sample was kept in solution for 7 days at  $20^\circ\text{C}$  and  $37^\circ\text{C}$ . The solution volume and weight of the samples were determined according to the recommendations of ISO 10993-5-2023 [70]. The  $\text{Ca}^{2+}$  content in the solution was determined using complexometric titration.

## 5. Conclusions

In this work, samples based on calcium phosphates were synthesized. The calcination of the synthesized samples at a temperature of  $900^\circ\text{C}$  led to the formation of hydroxyapatite and, in the case of using the PVP additive, to the formation of a two-phase powder: pyrophosphate and calcium phosphate. The presence of these two phases in the CPs sample can help improve the osteoinductive properties of the hydroxyapatite-based material by increasing the pH in the area where the material makes contact with bone apatite and promote the bioresorption of bone apatite [71,72]. The molar calcium–phosphate ratio, Ca/P, in the samples turned out to be close to the composition of tooth enamel. This indicates the promise of using these synthesized materials, HAP and CPs, in regenerative medicine and dentistry. It should be noted that PVP composite fibers with incorporated CPs particles are of independent interest for various applications since they have improved physical properties (strength, elasticity, etc.) compared to traditional composites [73]. Fiber diameter, specific surface area, pore size, and total pore volume significantly influence the diffusion of the liquid in which the nanofibers are immersed and influence the release of the bioactive substance according to the obtained solubility data in a physiological solution. The advantage of nanofiber materials is that their structure, namely, the fiber diameter, density, and thickness of the nanofiber layer, can be controlled by changing the process parameters of electrospinning [74].

**Author Contributions:** Conceptualization, M.V.P. and S.N.I.; methodology, M.V.P., S.N.I., R.P.Y., I.S.P. and I.V.S.; software, S.N.I., I.S.P. and I.V.S.; validation, M.V.P., S.N.I., I.S.P., A.N.G. and I.V.S.; formal analysis, M.V.P., S.N.I., R.P.Y., V.Y.B., I.V.S. and A.N.G.; data curation, M.V.P. and S.N.I.; writing—original draft preparation, M.V.P., S.N.I., R.P.Y., V.Y.B. and I.V.S.; writing—review and editing, M.V.P., S.N.I., R.P.Y., V.Y.B. and I.V.S.; visualization, M.V.P., S.N.I. and R.P.Y. All authors have read and agreed to the published version of the manuscript.

**Funding:** This research was funded by the Ministry of Science and Higher Education of the Russian Federation (No. FZEN-2023-0006).

**Institutional Review Board Statement:** Not applicable.

**Informed Consent Statement:** Not applicable.

**Data Availability Statement:** Data and information related to this study are available upon request.

**Acknowledgments:** This work was carried out using equipment available at the Laboratory of Advanced Nanobiotechnologies of Federal State Budgetary Educational Institution of Higher Education “Kuban State Agrarian University named after I.T. Trubilin” and Research and Educational Center of the Central Collective Use Center “Diagnostics of the Structure and Properties of Nanomaterials” of the Federal State Budgetary Educational Institution of Higher Education “Kuban State University”.

**Conflicts of Interest:** The authors declare no conflicts of interest.

## References

- Paňtak, P.; Czechowska, J.P.; Cichoń, E.; Zima, A. Novel double hybrid-type bone cements based on calcium phosphates, chitosan and citrus pectin. *Int. J. Mol. Sci.* **2023**, *24*, 13455. [[CrossRef](#)]
- Bakan, F.; Laçin, O.; Sarac, H. A novel low temperature sol-gel synthesis process for thermally stable nano crystalline hydroxyapatite. *Powder Technol.* **2013**, *233*, 295–302. [[CrossRef](#)]
- Chatakun, P.; Núñez-Toldrà, R.; López, E.J.D.; Gil-Recio, C.; Martínez-Sarrà, E.; Hernández-Alfaro, F.; Ferrés-Padró, E.; Giner-Tarrida, L.; Atari, M. The effect of five proteins on stem cells used for osteoblast differentiation and proliferation: A current review of the literature. *Cell Mol. Life Sci.* **2014**, *71*, 113–142. [[CrossRef](#)] [[PubMed](#)]
- Leontiev, V.K. Biologically active synthetic calcium-phosphate-containing materials for dentistry. *Stomatology* **1996**, *5*, 4–6.
- Kovylin, R.S.; Aleinik, D.A.; Fedyushkin, I.L. Modern porous polymeric implants: Preparation, properties, and application. High-molecular compounds. *Polym. Sci. Ser. C* **2021**, *63*, 33–53. [[CrossRef](#)]
- Kołodziejewska, B.; Figat, R.; Kolmas, J. Biomimetic apatite/natural polymer composite granules as multifunctional dental tissue regenerative material. *Int. J. Mol. Sci.* **2023**, *24*, 16751. [[CrossRef](#)] [[PubMed](#)]
- Zalewska, J.; Vivcharenko, V.; Belcarz, A. Gypsum-related lipact on antibiotic-laded composite based on highly porous hydroxyapatite—Advantages and disadvantages. *Int. J. Mol. Sci.* **2023**, *24*, 17178. [[CrossRef](#)]
- Pisareva, E.V.; Vlasov, M.Y.; Volova, L.T. Indicators of bone tissue turnover in rabbits with the introduction of «allogeneic hydroxyapatite». *News Samara Sci. Cent. Russ. Acad. Sci.* **2015**, *17*, 908–912.
- Pisareva, E.V.; Volova, L.T.; Tikhonova, T.V.; Vlasov, M.Y.; Sokolovskaya, A.B.; Golub, Y.V. Application of nanostructured allogeneic hydroxyapatite for the correction of osteoresorption. In *High Technologies, Fundamental and Applied Research in Physiology and Medicine*; Polytechnic University: St. Petersburg, Russia, 2012; pp. 20–22.
- Sevastyanov, V.I.; Kirpichnikov, M.P. *Biocompatible Materials*; MIA: Moscow, Russia, 2011.
- Papezhuk, M.V.; Pilunova, E.; Ivanin, S.N.; Yakupov, R.P. Synthesis of microcrystalline hydroxyapatite and production of fibers using the electrospinning method based on it. *Proc. Kola Sci. Cent. Russ. Acad. Sci. Ser. Tech. Sci.* **2023**, *14*, 192–196.
- Radulescu, D.-E.; Vasile, O.R.; Andronescu, E.; Fikai, A. Latest research of doped hydroxyapatite for bone tissue engineering. *Int. J. Mol. Sci.* **2023**, *24*, 13157. [[CrossRef](#)]
- Ducheyne, P.; Radin, S.; King, L. The effect of calcium phosphate ceramic composition and structure on in vitro behavior. I. Dissolution. *J. Biomed. Mater. Res.* **1993**, *27*, 25–34. [[CrossRef](#)]
- Moreno, E.; Gregory, T.; Brown, W. Preparation and Solubility of Hydroxyapatite. *J. Res. Natl. Bur. Stand. Sect. A Phys. Chem.* **1968**, *72*, 773–782. [[CrossRef](#)]
- Putlyaev, V.I.; Safronova, T.V. New generation of calcium phosphate materials: The role of phase and chemical composition. *Glass Ceram.* **2005**, *3*, 30–33.
- Gregory, T.M.; Moreno, E.C.; Patel, J.M.; Brown, W.E. Solubility of  $\beta$ -Ca<sub>3</sub>(PO<sub>4</sub>)<sub>2</sub> in the system Ca(OH)<sub>2</sub>-H<sub>3</sub>PO<sub>4</sub>-H<sub>2</sub>O at 5, 15, 25, and 37 °C. *J. Res. Natl. Bur. Stand. Sect. A Phys. Chem.* **1974**, *78*, 667–674. [[CrossRef](#)] [[PubMed](#)]
- Vereecke, G.; Lemaitre, S. Calculation of the solubility diagrams in the system Ca(OH)<sub>2</sub>-H<sub>3</sub>PO<sub>4</sub>-KOH-HNO<sub>3</sub>-CO<sub>2</sub>-H<sub>2</sub>O. *J. Cryst. Growth* **1990**, *104*, 820–832. [[CrossRef](#)]
- Fulmer, M.T.; Ison, I.C.; Hankermayer, C.R.; Constantz, B.R.; Ross, J. Measurements of the solubilities and dissolution rates of several hydroxyapatites. *Biomaterials* **2002**, *23*, 751–755. [[CrossRef](#)] [[PubMed](#)]
- Vamze, J.; Pilmane, M.; Skagers, A. Biocompatibility of pure and mixed hydroxyapatite and  $\alpha$ -tricalcium phosphate implanted in rabbit bone. *J. Mater. Sci. Mater. Med.* **2015**, *26*, 73. [[CrossRef](#)]
- Cheng, Y.; Zhao, G.; Liu, H. Histological evaluation of collagen-hydroxyapatite composite as osseous implants in the repair of mandibular defect. *Zhongguo Xiu Fu Chong Jian Wai Ke Za Zhi* **1998**, *12*, 74–76. [[PubMed](#)]
- Dhand, V.; Rhee, K.Y.; Park, S.J. The facile and low temperature synthesis of nanophase hydroxyapatite crystals using wet chemistry. *Mater. Sci. Eng. C* **2014**, *36*, 152–159. [[CrossRef](#)]
- McKay, W.F. Ceramic Fusion Implants and Compositions. U.S. Patent US6037519A, 14 March 2000.

23. Kumar, S.S.D.; Abrahamse, H. Advancement of nanobiomaterials to deliver natural compounds for tissue engineering applications. *Int. J. Mol. Sci.* **2020**, *21*, 6752. [[CrossRef](#)]
24. Torres-Martínez, E.J.; Bravo, J.M.C.; Medina, A.S.; González, G.L.P.; Gómez, L.J.V.A. Summary of electrospun nanofibers as drug delivery system: Drugs loaded and biopolymers used as matrices. *Curr. Drug Deliv.* **2018**, *15*, 1360–1374. [[CrossRef](#)]
25. Xue, J.; Wu, T.; Dai, Y.; Xia, Y. Electrospinning and electrospun nanofibers: Methods, materials, and applications. *Chem. Rev.* **2019**, *119*, 5298–5415. [[CrossRef](#)]
26. Nair, L.S.; Laurencin, C.T. Polymers as biomaterials for tissue engineering and controlled drug delivery. In *Tissue Engineering I*; Springer: Berlin/Heidelberg, Germany, 2006; Volume 102, pp. 47–90. [[CrossRef](#)]
27. Maitz, M.F. Applications of synthetic polymers in clinical medicine. *Biosurf. Biotribol.* **2015**, *1*, 161–176. [[CrossRef](#)]
28. Buzko, V.; Ivanin, S.; Goryachko, A.; Shutkin, I.; Pushankina, P.; Petriev, I. Magnesium spinel ferrites development for FDM 3D-printing material for microwave absorption. *Processes* **2023**, *11*, 60. [[CrossRef](#)]
29. Velasco Barraza, R.; Alvarez Suarez, A.S.; Villarreal Gomez, L.J.; Paz González, J.A.; Iglesias, A.L.; Vera Graziano, R. Designing a low-cost electrospinning device for practical learning in a bioengineering biomaterials course. *Rev. Mex. Ing. Bioméd.* **2016**, *37*, 7–16. [[CrossRef](#)]
30. Stafin, K.; Śliwa, P.; Piątkowski, M. Towards polycaprolactone-based scaffolds for alveolar bone tissue engineering: A biomimetic approach in a 3D printing technique. *Int. J. Mol. Sci.* **2023**, *24*, 16180. [[CrossRef](#)]
31. Prokopchuk, N.R.; Shashok, J.S.; Prishchepenko, D.V.; Melamed, V.D. (Review). Electrospinning of nanofibers from chitosan solution. *Polym. Mater. Technol.* **2015**, *1*, 36–56.
32. Shin, Y.M.; Hohman, M.M.; Brenner, M.P.; Rutledge, G.C. Electrospinning: A whipping fluid jet generates submicron polymer fibers. *Appl. Phys. Lett.* **2001**, *78*, 1149–1151. [[CrossRef](#)]
33. Prahasti, G.; Zulfiand, A.; Munir, M.M. Needleless electrospinning system with wire spinneret: An alternative way to control morphology, size, and productivity of nanofibers. *Nano Express* **2020**, *1*, 010046. [[CrossRef](#)]
34. Brydson, J.A. *Plastics Materials*; Elsevier: Amsterdam, The Netherlands, 1999.
35. Anunziata, O.A.; Maria, L.; Beltramone, M.R. Hydroxyapatite/MCM-41 and SBA-15 nano-composites: Preparation, characterization and applications. *J. Mater.* **2009**, *2*, 1508–1519. [[CrossRef](#)]
36. Kaimonov, M.R.; Safronova, T.V.; Filippov, Y.Y.; Shatalova, T.B.; Preobrazhenskii, I.I. Calcium phosphate powder for obtaining of composite bioceramics. *Inorg. Mater. Appl. Res.* **2021**, *12*, 34–39. [[CrossRef](#)]
37. Ivanin, S.N.; Buz'ko, V.Y.; Sokolov, M.E.; Magomadova, M.A.; Panyushkin, V.T. Structure and properties of the mixed-ligand complex compound of gadolinium stearate with benzoyltrifluoroacetone. *J. Struct. Chem.* **2021**, *62*, 563–570. [[CrossRef](#)]
38. Ivanin, S.N.; Panyushkin, V.T.; Buzko, V.Y.; Selivantev, Y.M.; Kostyrina, T.V. Synthesis, investigation, and molecular simulation of possible structures of a heteroligand complex of gadolinium stearate with acetylacetone. *J. Struct. Chem.* **2021**, *62*, 19–28. [[CrossRef](#)]
39. Berzina-Cimdina, L.; Borodajenko, N. Research of calcium phosphates using fourier transform infrared spectroscopy. In *Infrared Spectroscopy—Materials Science, Engineering and Technology*; InTech: Rijeka, Croatia, 2012; Volume 6, pp. 124–148.
40. Binitha, M.P.; Pradyumnan, P.P. Dielectric property studies of biologically compatible brushite single crystals used as bone graft substitute. *J. Biomater. Nanobiotechnol.* **2013**, *4*, 119–122. [[CrossRef](#)]
41. Boanini, E.; Gazzano, M.; Bigi, A. Ionic substitutions in calcium phosphates synthesized at low temperature. *Acta Biomater.* **2010**, *6*, 1882–1894. [[CrossRef](#)]
42. Buzko, V.; Babushkin, M.; Ivanin, S.; Goryachko, A.; Petriev, I. Study of electromagnetic shielding properties of composites based on glass fiber metallized with metal films. *Coatings* **2022**, *12*, 1173. [[CrossRef](#)]
43. Petriev, I.; Baryshev, M.G.; Voronin, K.A.; Lutsenko, I.S.; Pushankina, P.D.; Kopytov, G.F. Gas Transmission properties of Pd–Ag membranes coated with modifying layer. *Russ. Phys. J.* **2020**, *63*, 457–461. [[CrossRef](#)]
44. Buz'ko, V.Y.; Ivanin, S.N.; Shutkin, I.Y.; Goryachko, A.I.; Udodov, S.A.; Ozolin, A.V. Atomic composition, microstructure, and electromagnetic properties of schungite micropowder. *Condens. Matter Interphases* **2023**, *25*, 3–13. [[CrossRef](#)]
45. Petriev, I.; Pushankina, P.; Andreev, G.; Ivanin, S.; Dzhimak, S. High-performance hydrogen-selective Pd–Ag membranes modified with Pd–Pt nanoparticles for use in steam reforming membrane reactors. *Int. J. Mol. Sci.* **2023**, *24*, 17403. [[CrossRef](#)]
46. Schwarzenbach, G.; Flashka, G. *Complexometric Titration*; M.: Chemistry; U.S. Department of Energy: London, UK, 1970; p. 360.
47. Carrodegua, R.G.; Alonso, L.M.; García-Menocal, J.A.D.; Alonso, L.M.; Molins, M.P.G.; Manent, S.M.; Gil Mur, J.; Pérez, J.T.; Estany, J.A.P. Hydrothermal method for preparing calcium phosphate monoliths. *Mater. Res.* **2003**, *6*, 395–401. [[CrossRef](#)]
48. Kannan, S.; Goetz-Neunhoeffer, F.; Neubauer, J.; Ferreira, J.M.F. Ionic substitutions in biphasic hydroxyapatite and b-tricalcium phosphate mixtures: Structural analysis by rietveld refinement. *J. Am. Ceram. Soc.* **2008**, *91*, 1–12. [[CrossRef](#)]
49. Hughes, J.M.; Cameron, M.; Crowley, K.D. Structural variations in natural F, OH, and Cl apatites. *Am. Mineral.* **1989**, *74*, 870–876.
50. Kamiyama, T.; Hoshikawa, A.; Yashima, M.; Sakai, A. Crystal structure analysis of beta-tricalcium phosphate Ca<sub>3</sub>(PO<sub>4</sub>)<sub>2</sub> by neutron powder diffraction. *J. Solid State Chem.* **2003**, *175*, 272–277. [[CrossRef](#)]
51. Boudin, S.; Grandin, A.; Borel, M.M.; Leclaire, A.; Raveau, B. Redetermination of the β-Ca<sub>2</sub>P<sub>2</sub>O<sub>7</sub> structure. *Acta Crystallogr. Sect. C* **1993**, *49*, 2062–2064. [[CrossRef](#)]
52. Bian, J.; Kim, D.W.; Hong, K.S. Microwave dielectric properties of Ca<sub>2</sub>P<sub>2</sub>O<sub>7</sub>. *J. Eur. Ceram. Soc.* **2003**, *23*, 2589–2592. [[CrossRef](#)]
53. Parodi, J.A.; Hickok, R.L.; Segelken, W.G.; Cooper, J.R. Electronic paramagnetic resonance study of the thermal decomposition of dibasic calcium orthophosphate. *J. Electrochem. Soc.* **1965**, *112*, 688–692. [[CrossRef](#)]

54. Griesiute, D.; Garskaite, E.; Antuzevics, A.; Klimavicius, V.; Balevicius, V.; Zarkov, A.; Katelnikovas, A.; Sandberg, D.; Kareiva, A. Synthesis, structural and luminescent properties of Mn doped calcium pyrophosphate (Ca<sub>2</sub>P<sub>2</sub>O<sub>7</sub>) polymorphs. *Sci. Rep.* **2022**, *12*, 7116. [[CrossRef](#)]
55. Tazibt, N.; Kaci, M.; Dehouche, N.; Ragoubi, M.; Atanase, L.I. Effect of filler content on the morphology and physical properties of poly(lactic acid)-hydroxyapatite. *Compos. Mater.* **2023**, *16*, 809. [[CrossRef](#)]
56. Klee, W.E.; Engel, G. Infrared spectra of the phosphate ions in various apatite. *J. Inorg. Nucl. Chem.* **1970**, *32*, 1837–1843. [[CrossRef](#)]
57. Ivanin, S.N.; Buzko, V.Y.; Goryachko, A.I.; Panyushkin, V.T. Optical and magnetic properties of a heteroligand complex of gadolinium stearate with acetylacetone. *Russ. J. Phys. Chem. A* **2021**, *95*, 326–331. [[CrossRef](#)]
58. Papezhuk, M.V.; Volynkin, V.A.; Stroganova, T.A.; Usacheva, T.R.; Thi, L.P. Theoretical and experimental study of inclusion complex formation of β-cyclodextrin with some 1,4-diazepine derivatives. *Macroheterocycles* **2020**, *13*, 64–73. [[CrossRef](#)]
59. Pavlova, T.V.; Bavykina, T.Y. Comparative evaluation of the mineral composition and ultramicrostructure of dental tissues in norm and with caries. *Mod. Sci.-Intensive Technol.* **2009**, *12*, 15–18.
60. Teotia, A.K.; Raina, D.B.; Singh, C.; Sinha, N.; Isaksson, H.; Tägil, M.; Lidgren, L.; Kumar, A. Nano-hydroxyapatite bone substitute functionalized with bone active molecules for enhanced cranial bone regeneration. *ACS Appl. Mater. Interfaces* **2017**, *9*, 6816–6828. [[CrossRef](#)]
61. Safronova, T.V.; Putlyaev, V.I.; Shekhirev, M.A.; Kuztsov, A.V. Composite ceramics containing a bioresorbable phase. *Glass Ceram.* **2007**, *3*, 31–35. [[CrossRef](#)]
62. Kuczumow, A.; Chałas, R.; Nowak, J.; Smulek, W.; Jarzębski, M. Novel approach to tooth chemistry: Quantification of human enamel apatite in context for new biomaterials and nanomaterials development. *Int. J. Mol. Sci.* **2021**, *22*, 279. [[CrossRef](#)]
63. Veresov, A.G.; Putlyaev, V.I.; Tretyakov, Y.D. Chemistry of inorganic biomaterials based on calcium phosphates. *Russian Chem. J.* **2004**, *48*, 52–64.
64. Kokubo, T.; Kim, H.M.; Kawashita, M. Novel bioactive materials with different mechanical properties. *Biomaterials* **2003**, *24*, 2161–2175. [[CrossRef](#)]
65. Puleo, D.A.; Nanci, A. Understanding and controlling the bone–implant interface. *Biomaterials* **1999**, *20*, 2311–2321. [[CrossRef](#)]
66. Collins, A.M. Physical Techniques. In *Nanotechnology Cookbook*; Elsevier: Oxford, UK, 2012; pp. 205–253. [[CrossRef](#)]
67. Leonova, L.A.; Guzeeva, T.I.; Guzeev, V.V. Study of the synthesis process of hydroxyapatite. *Chem. Sustain. Dev.* **2010**, *18*, 107–110.
68. Liu, D.M.; Troczynski, T.; Tseng, W.J. Water-based sol-gel synthesis of hydroxyapatite: Process development. *Biomaterials* **2001**, *13*, 1721–1730. [[CrossRef](#)]
69. Goloshchapov, D.L.; Kashkarov, V.M.; Rumyantseva, N.A.; Seregin, P.V.; Len'shin, A.S.; Agapov, B.L.; Domashevskaya, E.P. Obtaining nanocrystalline hydroxyapatite by chemical precipitation using a biogenic source of calcium. *Condens. Media Interphase* **2011**, *13*, 427–441.
70. *ISO 10993-5-2023; Medical Devices. Assessment of the Biological Effects of Medical Devices. Part 5. Cytotoxicity Studies Using In Vitro Methods.* ISO: Geneva, Switzerland, 2023.
71. Safronova, T.V.; Putlyaev, V.I. Medical inorganic materials science in Russia: Calcium phosphate materials. *Nanosyst. Phys. Chem. Math.* **2013**, *4*, 24–47.
72. Gurin, A.N.; Komlev, V.S.; Fadeeva, I.V.; Barinov, S.M. Octacalcium phosphate—A precursor of biological mineralization, a promising osteoplastic material. *Dentistry.* **2010**, *4*, 65–72.
73. Tiwari, G.; Rai, A.K.; Tiwari, R. Cyclodextrins in delivery systems: Applications. *J. Pharm. Bioallied Sci.* **2010**, *2*, 72–79. [[CrossRef](#)]
74. Hrib, J.; Sirc, J.; Hobzova, R.; Hampejsova, Z.; Bosakova, Z.; Munzarova, M.; Michalek, J. Nanofibers for drug delivery—Incorporation and release of model molecules, influence of molecular weight and polymer structure. *Beilstein J. Nanotechnol.* **2015**, *6*, 1939–1945. [[CrossRef](#)]

**Disclaimer/Publisher's Note:** The statements, opinions and data contained in all publications are solely those of the individual author(s) and contributor(s) and not of MDPI and/or the editor(s). MDPI and/or the editor(s) disclaim responsibility for any injury to people or property resulting from any ideas, methods, instructions or products referred to in the content.